ELSEVIER

Available online at www.sciencedirect.com

ScienceDirect

Cement & Concrete Composites 30 (2008) 227–238

Cement & Concrete Composites

www.elsevier.com/locate/cemconcomp

Chloride-induced reinforcement corrosion and concrete cracking simulation

Dong Chen, Sankaran Mahadevan *

Department of Civil and Environmental Engineering, Vanderbilt University, Nashville, TN 37235, USA

Received 22 August 2005; received in revised form 24 July 2006; accepted 24 October 2006
Available online 29 April 2007

Abstract

This paper develops an integrated computational methodology for chloride-induced degradation assessment of reinforced concrete structures by considering all three phases of the deterioration process. The chloride penetration process is simulated using a finite element-based method by following an analogous transient thermal analysis. A reinforcement corrosion and rust expansion model based on Faraday's law is developed, and the rust expansion is characterized by an equivalent time-varying radial displacement boundary condition. Two established corrosion rate models – the constant model and the dynamic model – are included in the rust expansion model. Finite element analysis with a smeared cracking approach is implemented to simulate the rust expansion and the associated concrete cracking process. Simulation results are presented for a reinforced concrete slab exposed to a constant chloride environment.

Keywords: Chloride penetration; Reinforcement corrosion; Rust expansion; Cracking; Durability; Service life

1. Introduction

The durability of reinforced concrete structures is impacted by the chloride penetration and susceptibility of the reinforcement to chloride-induced corrosion, when exposed to marine environment or deicing salts. Once the chloride content at the reinforcement reaches a threshold value and enough oxygen and moisture are present, the reinforcement corrosion will be initiated. Corrosion products then accumulate in the concrete–steel interface transition zone (ITZ), generate expansive pressure on the surrounding concrete, and cause crack initiation and propagation.

Quality concrete is able to prevent the embedded reinforcing steel from potential corrosion in three ways. First, hydration products of cement in concrete form a high alkaline pore solution environment, where the passivated film covering the steel surface remains chemically stable enough to protect reinforcing steel from corroding [1]. Second, quality concrete usually possesses low porosity and permeability, which greatly minimizes the penetration of corrosion-induced agents (such as chloride, carbon dioxide, oxygen, moisture, etc.) through porous concrete. Third, the high electrical resistivity of quality concrete restricts the corrosion by reducing the electrical current flow between the anodic and cathodic sites. However, quality concrete cannot always be attained in practice, especially when concrete with initial flaws (including micropores and microcracks) is exposed to adverse environments. Chloride penetration may result in the accumulation of chloride content at reinforcement to such a level that the high alkaline environment is destroyed and then the passivated film on the steel surface is disrupted [2,3]. Once enough oxygen and moisture are present, the reinforcement corrosion will be initiated.

After the initiation of corrosion, the corrosion products (including various iron oxides) with relatively lower density occupy much more volume than the original iron. As the corrosion progresses, the corrosion products accumulate in ITZ and generate expansive pressure on the surrounding

---

* Corresponding author. Tel.: +1 615 322 3040; fax: +1 615 322 3365.
E-mail address: sankaran.mahadevan@vanderbilt.edu (S. Mahadevan).

0958-9465/$ - see front matter © 2007 Elsevier Ltd. All rights reserved.
doi:10.1016/j.cemconcomp.2006.10.007

concrete. The pressure builds up to such high level that cause crack initiation and propagation. In addition to the cracking in surrounding concrete, chloride-induced reinforcement corrosion results in loss of the concrete–steel interface bond, and reduction of the cross-sectional area of reinforcement, thus reducing the load carrying capacity of concrete structure [4].

The entire chloride-induced reinforcement corrosion process of reinforced concrete structures can be divided roughly into three phases as shown in Fig. 1. The first phase is characterized by the chloride penetration, during which the chloride diffuses gradually from the concrete surface through the concrete cover toward the reinforcement. When the chloride content at reinforcement reaches a threshold value to initiate the corrosion process at time $t_{\text{initiation}}$, the second phase is assumed to begin. The second phase is dominated by the reinforcement rust expansion, during which the rust (i.e., the corrosion products) accumulates in the concrete–steel ITZ. Once voids in ITZ are occupied completely with the rust at time t_{stress}, further rust accumulation will trigger expansive stress and then cracking in the surrounding concrete, which indicates the start of the third phase. During the third phase, the rust expansion-induced cracks propagate in concrete surrounding the reinforcing steels until some critical failure mode, such as the spalling or delamination of concrete cover, occurs at time t_{spalling}, which indicates the end of the third phase.

Among the three phases, the first phase usually lasts for a relatively long period, depending on corrosion resistance of the reinforcement, thickness and quality of the concrete cover, ambient chloride content, etc. The second phase is much shorter than the first one, which is determined mainly by the porosity of ITZ. The third phase is the shortest one since the rust expansion-induced cracks propagate rapidly through the surrounding concrete. Considering only the chloride-induced reinforcement corrosion, the entire service life may be defined as the sum of all three phases. Under specified design requirements, the termination of service life can also be defined by an acceptable level of corrosion indicated on the vertical axis of Fig. 1.

The chloride-induced reinforcement corrosion and cracking patterns corresponding to the three phases defined in Fig. 1 are illustrated in Fig. 2 [5].

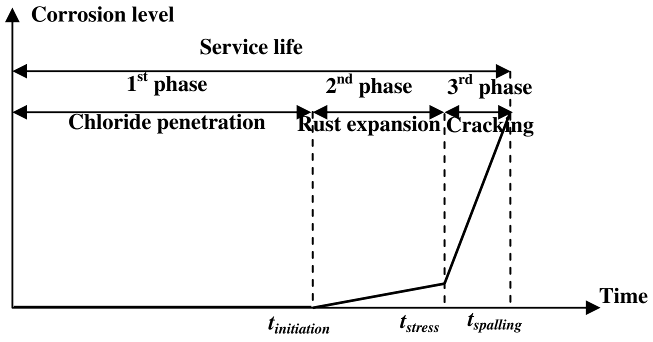

Fig. 1. Chloride-induced reinforcement corrosion process.

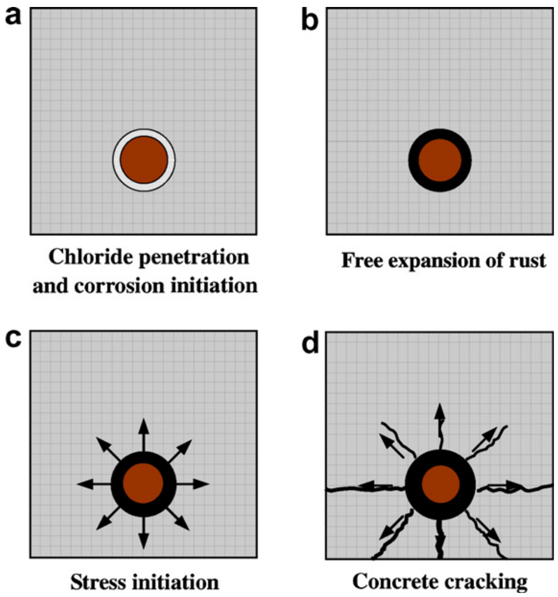

Chloride penetration and corrosion initiation

Free expansion of rust

Stress initiation

Concrete cracking

Fig. 2. Chloride-induced reinforcement corrosion and cracking patterns.

During the past decades, various empirical and numerical models have been proposed to estimate the deterioration caused by the chloride-induced reinforcement corrosion and to predict the service life of the reinforced concrete structure. Tuutti [6] suggested a model to predict the service life, where the maximum acceptable corrosion level is related to the appearance of cracks. The deterioration process consists of two periods: initiation and propagation. The initiation period can be estimated as the time required for chloride to reach the reinforcement surface and trigger active corrosion, while the propagation period can be taken as the time elapsed until repair becomes mandatory. Cady and Weyers [7] developed a deterioration model to estimate the remaining life of concrete bridge components in corrosive environment, assuming that chloride-induced reinforcement corrosion is the main cause of deterioration. The model predicts bridge deck deterioration level in terms of percentage area of the entire deck. Based on the physical mechanism for corrosion of reinforcing steel in concrete exposed to marine environment, Bazant [8,9] proposed a mathematical model to determine the time to cracking of the concrete cover. In this model, the time to cracking is assumed to be a function of corrosion rate, cover depth, spacing of steel rebars, and mechanical properties of concrete. Based on field and laboratory observations, Morinaga [10] developed an empirical model to predict the time to cracking. It is assumed that concrete cracking will first occur when there is a critical quantity of corrosion products forming on the reinforcement. Liu and Weyers [5] suggested a similar corrosion-cracking model to compute the time to cracking using the critical amount of rust, which consists of the amount of corrosion products needed to fill the ITZ voids plus the amount of corrosion products needed to generate sufficient tensile stresses to crack the cover concrete. In summary, a realistic numerical model for chloride-induced corrosion process should be able to closely track each of the corrosion stages shown in Fig. 2.

This paper develops an integrated computational methodology to simulate the chloride-induced degradation process of reinforced concrete structures, where all three phases of the deterioration process are considered separately.

2. Chloride penetration simulation

Simulation of the chloride penetration through concrete is implemented using a finite element-based method by following an analogous transient thermal analysis. The influences of the chloride binding capacity of concrete, age of concrete, local chloride content, and temperature variation on chloride penetration are considered simultaneously by adjusting the chloride diffusivity of concrete through a multifactor law.

Both free chloride and bound chloride exist in concrete. Chloride-induced corrosion is related only to the free chloride, since the bound chloride is immovable and cannot initiate the corrosion [6]. Based on mass conservation, the chloride penetration process is formulated as:

$$\frac{\partial C_f}{\partial t} = \mathrm{div}[D \cdot \mathrm{grad}(C_f)] - \frac{1}{\omega_e} \cdot \frac{\partial C_b}{\partial t} \tag{1}$$

where C_f is the free chloride, C_b is the bound chloride, D is the actual chloride diffusivity, ω_e is the free moisture content. Following Xi and Bazant [11] and Martin-Perez et al. [12], the concrete is assumed to be completely saturated and ω_e is constant. Eq. (1) can be reduced further to a modified form of Fick's second law as:

$$\frac{\partial C_f}{\partial t} = \mathrm{div}[D^* \cdot (C_f)] \tag{2}$$

where D^* is the apparent chloride diffusivity and can be expressed as:

$$D^* = D \cdot F_1(C_b) \tag{3}$$

$$F_1(C_b) = \frac{1}{1 + \frac{1}{\omega_e} \cdot \frac{\partial C_b}{\partial C_f}} \tag{4}$$

where $\frac{\partial C_b}{\partial C_f}$ is referred to as the chloride "binding capacity" of concrete by Nilsson et al. [13], $F_1(C_b)$ is the influencing factor due to the chloride binding capacity of concrete. The chloride binding capacity reflects the relationship between bound chloride and free chloride, and can be obtained using appropriate chloride binding isotherm models. The Freundlich binding isotherm model [12] is adopted in this paper as:

$$C_b = \alpha \cdot C_f^{\beta} \quad \frac{\partial C_b}{\partial C_f} = \alpha\beta C_f^{\beta-1} \quad F_1(C_b) = \frac{1}{1 + \frac{\alpha\beta C_f^{\beta-1}}{\omega_e}} \tag{5}$$

where the model parameters $\alpha = 1.037$ and $\beta = 0.36$ are determined through interpolation from suggested values [14] for OPC concrete with WCR = 0.5.

The dependence of the actual chloride diffusivity D on the age of concrete t, the local chloride content C_f, and the temperature T are included in a multifactor law as:

$$D = D_0 \cdot F_2(t) \cdot F_3(C_f) \cdot F_4(T) \tag{6}$$

where D_0 is referred to as the reference chloride diffusivity when all influencing factors assume values of unity, $F_2(t)$ denotes the influence of the age of concrete, $F_3(C_f)$ represents the influence of the free chloride content, $F_4(T)$ indicates the influence of temperature.

D_0 can be estimated as a function of the water to cement ratio [15] as

$$\log_{10} D_0 = 6.0 \cdot \mathrm{WCR} - 13.84 \tag{7}$$

With the water to cement ratio WCR = 0.5, D_0 assumes a value of 14.45×10^{-12} m^2/s.

According to Martin-Perez et al. [16], $F_2(t)$ takes the form

$$F_2(t) = \left(\frac{t_{\mathrm{ref}}}{t}\right)^m \tag{8}$$

where t_{ref} is the reference age from which D_0 is derived (assumed to be 1 year herein), t is the actual age of concrete (year), and the empirical parameter m assumes a value of 0.04.

$F_3(C_f)$ follows Xi and Bazant [11] and Kong et al. [17] as

$$F_3(C_f) = 1 - k \cdot (C_f)^n \tag{9}$$

where the empirical parameters $k = 8.333$, and $n = 0.5$.

Based on Arrhenius' law, both Martin-Perez et al. [16] and Kong et al. [17] suggested $F_4(T)$ as

$$F_4(T) = \exp\left[\frac{E}{R}\left(\frac{1}{T_{\mathrm{ref}}} - \frac{1}{T}\right)\right] \tag{10}$$

where E is the activation energy of the chloride diffusion process (kJ/mol), assuming a value of 44.6 for WCR = 0.5; R is the gas constant (=8.314 J/K mol), T_{ref} is the reference temperature at which D_0 is determined (=296 K), and T is the actual absolute temperature in concrete (K).

Considering the dependence of the chloride diffusivity on various influencing variables as well as the time-varying boundary conditions, the nonlinear partial differential equation, Eq. (2), is solved numerically using finite element method, where the chloride penetration process is solved in space as a boundary-value problem and in time as an initial-value problem. Due to the availability of transient thermal analysis in an existing finite element software, the proposed finite element method can be implemented by following an analogous transient thermal analysis. The numerical simulation procedure for the chloride penetration is summarized in Fig. 3.

The heat transfer and chloride penetration processes are defined as two individual physics environments first, where the 8-node 3-D thermal element Solid70 with one DOF of temperature at each node is selected for both processes. The physics environment functions like an independent module, where finite element types, constant material

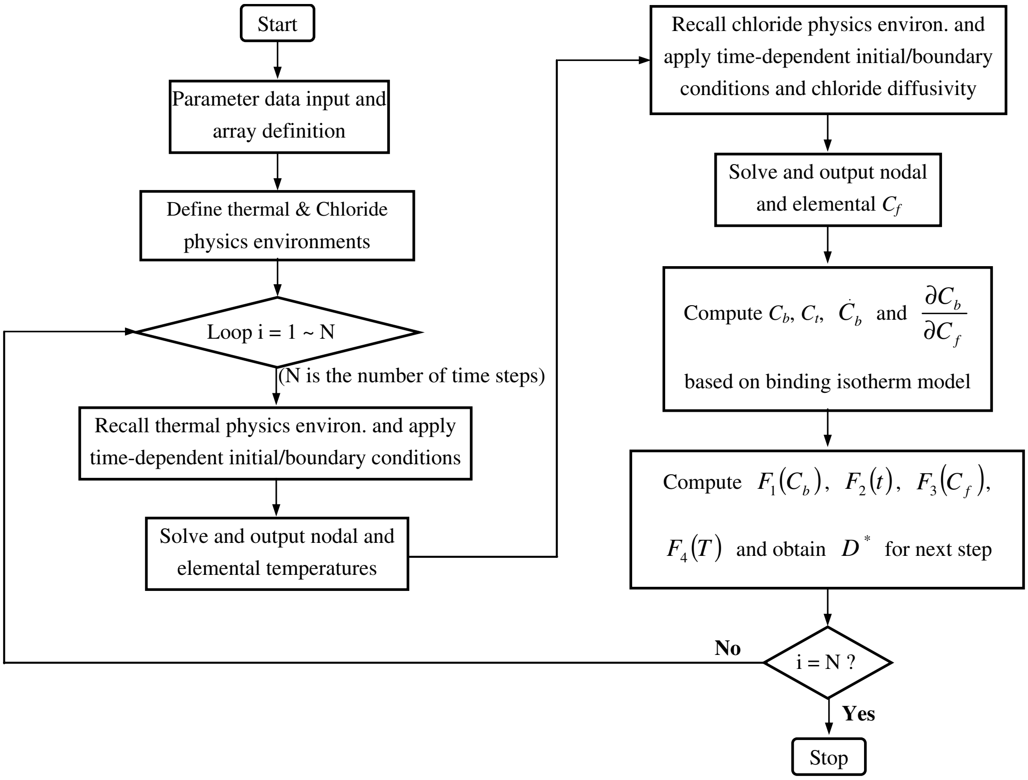

Fig. 3. Simulation procedure of chloride penetration.

properties, geometric model, fixed boundary conditions, as well as meshing of the solid model are defined separately. Next, a coupled multi-physics analysis is utilized to call each physics environment in turn, apply the time-dependent loads and material properties, and then perform the simulation of heat transfer and chloride penetration processes iteratively within each time step. Each time step is divided into a number of substeps, which may vary with each physics environment and each time step. An automatic time stepping (i.e., adaptive loading) scheme is adopted to ensure the substep size is appropriate enough to achieve desired convergence. To account for the influences of various factors on chloride penetration, the output of two processes at the ith time step – the age of concrete, the distribution of the temperature and free chloride content, as well as the associated chloride binding capacity – are extracted to adjust the apparent chloride diffusivity of each finite element at the next $(i+1)$th time step through a multifactor law. All output results are classified and stored in individual arrays at each time step. A self-programmed code in ANSYS Parametric Design Language (APDL) is required to implement the flow chart and the proposed meth- odology.

3. Corrosion-induced reinforcement rust expansion model

Reinforcement corrosion is essentially an electrochemical process, at the anode iron is oxidized to iron ions that pass into solution, and at the cathode oxygen is reduced to hydroxyl ions. The anode and the cathode form a corrosion cell, with the flow of electrons in the steel and of ions in the concrete pore solution [6,18,19].

Depending on various factors such as the pH value of the pore solution, the availability of oxygen and moisture, the content of aggressive agents, etc., the corrosion products possess complex stochiometry and may expand by about 4–6 times the original volume of iron. When compared with the parent metal iron, the characteristic physical properties of the typical corrosion products are summarized as shown in Table 1.

Two corrosion products are generally thought to be dominant – ferrous hydroxide $Fe(OH)_2$ and hydrated red rust $Fe(OH)_3$ [20,21]. For simplicity, this paper follows a general practice to represent the density of the corrosion product ρ_r as a fixed fraction of that of iron ρ_s as:

$$\rho_r = \rho_s/\gamma \tag{11}$$

where γ assumes a constant value of 2.17, when half the corrosion products is assumed to be $Fe(OH)_3$, and the other half is $Fe(OH)_2$ [20,21].

The mass of iron consumed M_s (g) is related to the amount of current I_{corr} (A) that flows through the electrochemical corrosion cell. The corrosion process can be formulated using Faraday's law as:

$$\frac{dM_s}{dt} = \frac{I_{corr}A}{nF} \tag{12}$$

where $A = 55.85$ g/mol is the atomic weight of the ion corroded, and Faraday's constant $F = 96{,}500$ C/mol. The

Table 1
Characteristic relative volume ratios of corrosion products

Corrosion product	Fe	FeO	Fe_3O_4	Fe_2O_3	$Fe(OH)_2$	$Fe(OH)_3$	$Fe(OH)_3 \cdot 3H_2O$
Relative volume ratio [17]	1.0	1.7	2.0	2.1	3.6	4.0	6.2
Molecular weight	56	72	232	160	90	107	161
Density ($\times 10^3$ kg/m^3)	7.85	5.93	16.24	10.67	3.50	3.75	3.64
Specific volume (g/cm^3)	0.127	0.169	0.062	0.094	0.286	0.267	0.275
Relative specific volume	1.0	1.32	0.48	0.74	2.24	2.09	2.16

valency of the reaction empirically assumes a value of $n = 2.5$ ($n = 2$ for $Fe(OH)_2$, and $n = 3$ for $Fe(OH)_3$) [20,22]. Thus, Faraday's law can be reduced further as:

$$\frac{dM_s}{dt} = 2.315 \times 10^{-4} \cdot I_{corr} \quad (g/s) \tag{13}$$

M_s can be obtained by integrating $\frac{dM_s}{dt}$ over time since the initiation of corrosion. The corresponding mass of corrosion products generated M_r (g) is expressed as:

$$M_r = M_s / r_m \tag{14}$$

where r_m ranges between 0.523 for $Fe(OH)_3$ and 0.622 for $Fe(OH)_2$, and assumes a value of 0.5685 [5,20].

Faraday's law forms the foundation for existing reinforcement corrosion models that assume a constant rate of iron consumption and rust generation. To model its mechanical effects, a corrosion-induced rust expansion model is proposed as illustrated in Fig. 4, where D_b is the original diameter of steel bar, D_{rb} is the reduced diameter of steel bar after corrosion, and D_{eb} is the corresponding diameter of rust expansion front.

The corrosion current density i_{corr} is defined as the corrosion current per unit steel surface. A relationship between I_{corr} (A) and i_{corr} (A/m^2) can be established as:

$$I_{corr} = \begin{cases} \pi \cdot D_b \cdot i_{corr} \cdot L & (t = 0) \\ \pi \cdot D_{rb} \cdot i_{corr} \cdot L & (t > 0) \end{cases} \tag{15}$$

where L is the length of the corroded steel bar.

The mass and volume of iron corroded per unit length (i.e., $L = 1.0$ m) of the steel bar are obtained as:

$$\Delta M_s = 2.315 \times 10^{-4} \cdot I_{corr} \cdot \Delta t = \begin{cases} 2.315 \times 10^{-4} \cdot \pi \cdot D_b \cdot i_{corr} \cdot \Delta t & (t=0) \\ 2.315 \times 10^{-4} \cdot \pi \cdot D_{rb} \cdot i_{corr} \cdot \Delta t & (t>0) \end{cases} \quad (g/m) \tag{16}$$

$$\Delta V_s = \frac{\Delta M_s}{\rho_s} = \begin{cases} \frac{5.90}{2} \times 10^{-11} \cdot \pi \cdot D_b \cdot i_{corr} \cdot \Delta t & (t=0) \\ \frac{5.90}{2} \times 10^{-11} \cdot \pi \cdot D_{rb} \cdot i_{corr} \cdot \Delta t & (t>0) \end{cases} \quad (m^3/m) \tag{17}$$

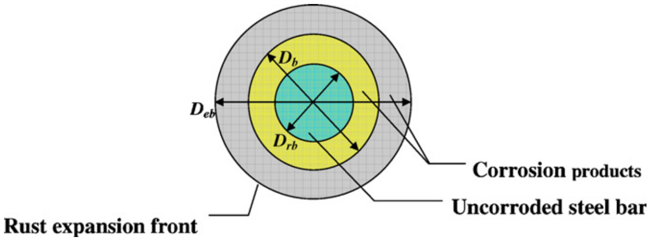

Fig. 4. Corrosion-induced rust expansion model.

Correspondingly, the outward volume expansion is derived to be the difference of the volume of rust generated and the volume of iron corroded as:

$$\Delta V = \Delta V_r - \Delta V_s = \frac{\Delta M_r}{\rho_r} - \frac{\Delta M_s}{\rho_s} = \Delta M_s \left[\frac{\Delta M_r}{\Delta M_s} \frac{1}{\rho_r} - \frac{1}{\rho_s} \right] \tag{18}$$

$$= \begin{cases} \frac{16.514}{2} \times 10^{-11} \cdot \pi \cdot D_b \cdot i_{corr} \cdot \Delta t & (t = 0) \\ \frac{16.514}{2} \times 10^{-11} \cdot \pi \cdot D_{rb} \cdot i_{corr} \cdot \Delta t & (t > 0) \end{cases} \quad (m^3/m)$$

Subsequently, D_{rb} and D_{eb} at the ith time step can be derived as:

$$D_{rb} = D_b - \sum_{n=1}^{i} 5.90 \times 10^{-11} \cdot i_{corr,n} \cdot \Delta t_n \quad (m) \tag{19}$$

$$D_{eb} = D_b + \sum_{n=1}^{i} 16.514 \times 10^{-11} \cdot \frac{D_{rb,n-1}}{D_{eb,n-1}} \cdot i_{corr,n} \cdot \Delta t_n \quad (m) \tag{20}$$

Thus, the time-dependent radial displacement on the rust expansion front surface at the ith time step can be expressed as:

$$u_r = \frac{D_{eb} - D_b}{2} = \sum_{n=1}^{i} 8.257 \times 10^{-11} \cdot \frac{D_{rb,n-1}}{D_{eb,n-1}} \cdot i_{corr,n} \cdot \Delta t_n \quad (m) \tag{21}$$

So far, a corrosion-induced reinforcement rust expansion model has been developed as shown in Eq. (21). It is convenient to impose the transient radial displacement boundary condition on the nodes along the concrete–steel interface of a finite element model. It should be emphasized that the proposed method is only a simplification. As rust expansion-induced concrete cracking progresses, steel bar may debond gradually from surrounding concrete. The displacement response of the concrete surrounding the steel bar thus becomes less and less axisymmetric such that the imposed radial displacement on the finite element nodes might artificially affect the cracking pattern.

4. Corrosion rate model

It can be observed in Eq. (21) that i_{corr} is the only factor controlling the corrosion-induced reinforcement rust expansion process. In this case, i_{corr} is called the corrosion rate by several researchers. Cady and Weyers [7] regarded the corrosion rate as the key to predicting the time to cracking. A sensitivity analysis on Bazant's model [8,9] indicated that the corrosion rate is the most significant parameter in determining the time to cracking of the cover concrete.

Several corrosion rate models have been proposed in the literature. In this paper, two established corrosion rate models – the constant model and the dynamic model – are combined with the reinforcement rust expansion model proposed in Section 3. Two sets of simulation results based on the two corrosion rate models are obtained and compared with each other.

Andrade et al. [23] classified the corrosion risk according to the mean annual value of corrosion rate i_{corr}, where constant corrosion rates are assigned to concrete structure under corresponding service conditions. Both Hansen and Saouma [24] and Hong [25] used similar constant corrosion rate models to calculate the decreasing diameter of corroded steel bar. The constant corrosion rate model adopted in this paper uses the value of $i_{\mathrm{corr}} = 1\ \mu\mathrm{A/cm}^2$ corresponding to a moderate corrosion risk [23,26].

However, the constant corrosion rate model may not always be applicable, especially in a highly varying aggressive environment. Jung et al. [22] expressed the corrosion rate as an exponential function of chloride content, relative humidity, and cover depth. Based on available chloride corrosion database (2927 measurements from seven series of chloride contaminated specimens, up to five years of outdoor exposure), Liu and Weyers [27] proposed a nonlinear regression model, in which corrosion rate varies with chloride content, temperature, ohmic resistance, and active corrosion time. This dynamic corrosion rate model is adopted in this paper as:

$$i_{\mathrm{corr}} = 0.926 \cdot \exp\left[7.98 + 0.7771\ln(1.69C_{\mathrm{t}}) - \frac{3006}{T} - 0.000116R_{\mathrm{c}} + 2.24t^{-0.215}\right] \quad (22)$$

where i_{corr} is the corrosion current density ($\mu\mathrm{A/cm}^2$), C_{t} is the total chloride content (kg/m^3 of concrete), T is temperature at the depth of reinforcement (K), R_{c} is the ohmic resistance of the cover concrete (ohm) and t is corrosion time (year).

Following the computational methodology proposed in Section 2, the total chloride content C_{t} and temperature T at the depth of reinforcement can be obtained. As to the ohmic resistance of the cover concrete R_{c}, Liu [28] established a regression relationship between the resistance of concrete and total chloride content for outdoor specimens as:

$$R_{\mathrm{c}} = \exp[8.03 - 0.549\ln(1 + 1.69C_{\mathrm{t}})] \quad (23)$$

Therefore, the dynamic corrosion rate model in Eq. (22) can be utilized conveniently in simulating the corrosion-induced reinforcement rust expansion process.

According to Thoft-Christensen [21,29–31], there is a porous zone around the concrete–steel interface caused by the transition from cement paste to steel, entrapped/entrained air voids, and corrosion products diffusing into the capillary voids in the cement paste. The volume of this porous zone is directly related to the surface area of reinforcement, water–cement ratio, degree of hydration, and degree of consolidation. As the corrosion is initiated on the surface of the steel, the porous zone will be gradually filled with the rust. After the total amount of generated rust exceeds the amount needed to fill the porous zone around the steel at t_{stress}, expansive pressure is caused on the surrounding concrete. The process of filling the porous zone is illustrated in Fig. 2b.

Very close to the steel bars the concrete porosity is close to unity, but the porosity decreases with the distance from the bars. The porosity is typically of the order of 0.5 at about 10–20 μm distance from the bar, which means the porous zone is very narrow [29,30]. Let δ_{por} be the thickness of an equivalent zone with porosity unit one around the steel bar. Based on the two established corrosion rate models, a recursive algorithm is required to apply the proposed reinforcement rust expansion model Eq. (21), and compute the time needed to fill the porous zone around the steel bar.

5. Cracking simulation

There usually exist two approaches to simulate the concrete cracking. Based mainly on fracture mechanics [32,33], the discrete cracking approach regards the crack propagation as the result of stress singularity or strain energy release at the tip of crack. Cracks are treated directly as geometric discontinuities, where the intact portion of concrete is generally assumed to behave elastically, while the crack propagation is modeled by changing the topology of the finite element model. The separation of two crack faces may be accomplished by introducing additional nodes and remeshing the local domain. Adaptive remeshing is required to implement the simulation.

Based on conventional solid mechanics, the smeared cracking approach describes the cracked concrete as a fictitious continuum. Cracks are assumed to be spatially distributed over the entire volume represented by finite element. The stiffness matrix of each concrete element is modified accordingly to accommodate the mechanical degradation due to cracking. Without changing the topology of finite element model, this approach proves efficient when incorporated in finite element analysis [34]. Mandke and Smalley [35] and Kachlakev et al. [36] modeled concrete cracking under mechanical loads using this approach. Saouma and Chang [37] followed the same approach to simulate the reinforced concrete deterioration due to reinforcement corrosion, where the forced displacement boundary conditions are applied on the crack surfaces.

In spite of some potential limitations (including sensitivity to mesh size, etc.), a smeared cracking approach combined with finite element analysis to model the crack propagation process is feasible due to its ease of implementation. Moreover, crack propagation paths can be tracked roughly. The finite element software ANSYS is adopted as illustration to simulate the mechanical response of concrete due to corrosion-induced reinforcement rust expansion after t_{stress}. A 3-D concrete element Solid65 is used to simulate the subsequent expansive stress and crack propagation. This solid element has eight nodes with three DOFs at each node – translations in the nodal x, y and z directions. The element allows plastic deformation, cracking in tension in three orthogonal directions, shear transfer capacity, and crushing in compression [38].

A uniaxial stress–strain relationship model of concrete is required to characterize its nonlinear mechanical properties. Developing an appropriate constitutive model for concrete is challenging, and substantial efforts were made to propose various models in the past [39,40]. In this paper, a constitutive model with the compression part following a perfectly plastic model and the tension part observing a linear elastic model is adopted. The ascending part of the compression constitutive relationship curve follows the Desayi and Krishnan model [39] as:

$$\sigma = \frac{E_c \varepsilon}{1 + (\varepsilon/\varepsilon_0)^2} \tag{24}$$

where $\varepsilon_0 = \frac{2f'_c}{E_c}$, E_c is the elastic modulus, f'_c is the ultimate compressive strength, f_t is the ultimate tensile strength. After the ultimate compressive strength f'_c is reached, a perfectly plastic behavior is assumed till crushing failure occurs at the ultimate strain ε_{cu}.

To assess the initiation of failure and identify the corresponding failure modes (including cracking and crushing) of each concrete element, the Willam and Warnke failure criterion [41] under multi-axial stress state is adopted herein. In concrete, cracking occurs when the principal tensile stress in any one direction lies outside the 3-D failure surface. Crushing occurs when all principal stresses are compressive and lie outside the failure surface. As either failure mode occurs, the stiffness matrix of that concrete element is modified accordingly to consider the mechanical degradation.

So far, a comprehensive simulation procedure has been developed for simulating the all three phases of the chloride-induced degradation process separately, as summarized in Fig. 5.

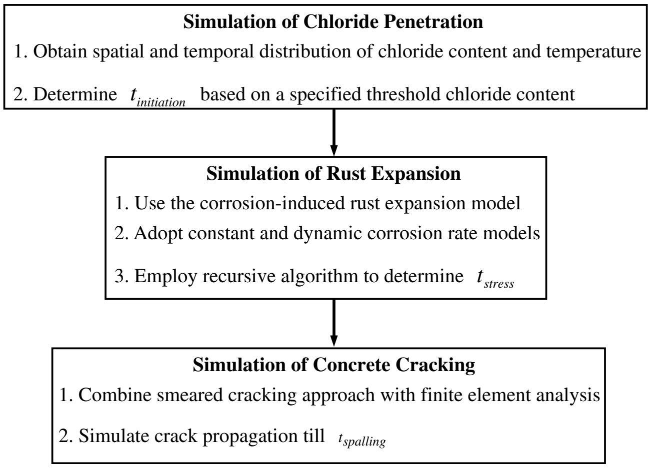

Fig. 5. Simulation of chloride-induced degradation.

It should be mentioned that the adopted constant and dynamic corrosion rate models do not explicitly consider the presence of cracking. Since the corrosion rate usually increases with the more direct exposure of steel bar to aggressive environment through cracks, the obtained time to spalling t_{spalling} might be not conservative.

6. Numerical example

An initially chloride-free reinforced concrete slab (Fig. 6) is illustrated to implement the proposed computational methodology, where boundary conditions of constant chloride content 3.5 kg/m^3 of concrete and annually varying ambient temperature $T_{\mathrm{ambient}} = 15 + 10 \cdot \sin(2\pi \cdot t)$ °C are applied on the bottom surface (*Note*: t is time elapsed in years). Considering the symmetric and repetitive geometric characteristics of the concrete slab and the initial/boundary conditions, only a representative part of the concrete slab as Fig. 7 is isolated to perform the simulation.

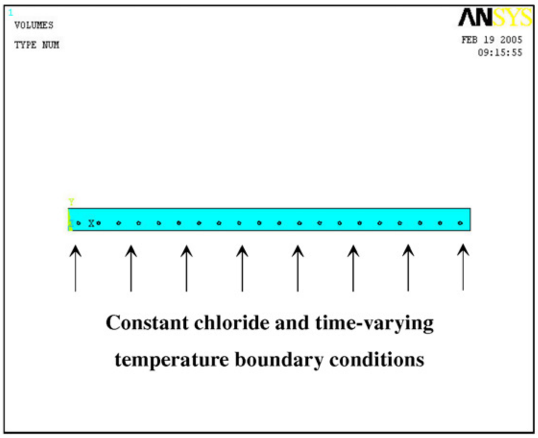

Fig. 6. Boundary conditions.

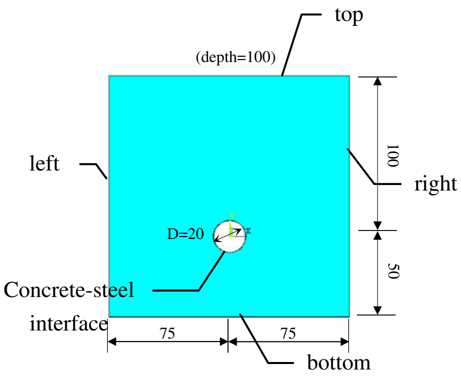

Fig. 7. Cross-section of concrete slab.

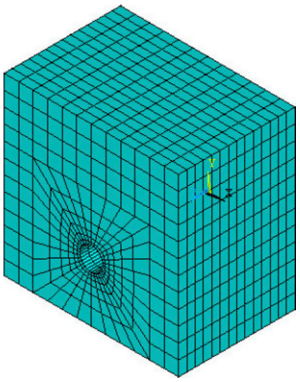

Fig. 8. Finite element model.

The finite element model of the representative part of concrete slab is shown in Fig. 8, which is utilized in simulating not only the chloride penetration but also the subsequent reinforcement rust expansion and concrete cracking.

Following the computational method proposed in Section 2, the time-dependent chloride content and temperature at the depth of the reinforcement are obtained as shown in Figs. 9 and 10, respectively. Since the presented example addresses a nearly one-dimensional problem, and the ambient temperature fluctuates so slowly that the internal temperature can always achieve equilibrium with the ambient temperature, the nodal temperature history can thus be obtained by directly prescribing the temperature fluctuation of the nodes. However, this may not apply to practical concrete structures with arbitrary geometries exposed to randomly varying ambient temperature. Hence, the proposed 3-D finite element-based methodology is required to obtain the temporal and spatial distribution of nodal temperature.

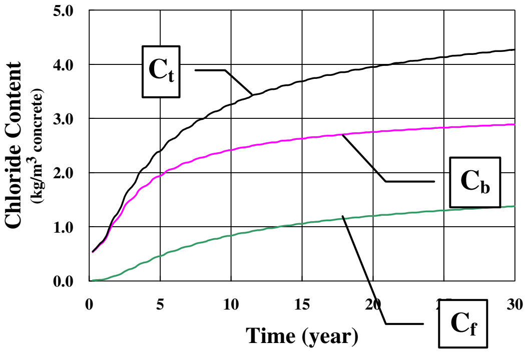

Fig. 9. Chloride content history.

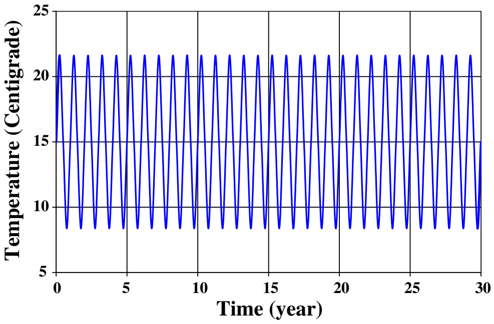

Fig. 10. Temperature history.

The threshold chloride content to initiate the reinforcement corrosion is controversial, since it is affected by various factors, such as water to cement ratio of the concrete, mixture proportions of the concrete, relative humidity, temperature, pH value of the pore solution, sulfate content, etc. [42–45]. According to Stewart and Rosowsky [26], the values of the threshold chloride content are uniformly distributed within the range of 0.6–1.2 kg/m^3 of concrete. If the value of the threshold chloride content is assumed to be 0.9 kg/m^3 of concrete, then the corrosion initiation time $t_{\text{initiation}}$ is determined to be 11.25 years.

Thoft-Christensen [21] assumes that δ_{por} has a mean value of 12.5 μm. Employing proposed reinforcement rust expansion model Eq. (21) with the constant corrosion rate model, it takes 0.48 year after $t_{\text{initiation}}$ to completely fill the porous zone; and it takes 0.37 years with the dynamic corrosion rate model.

$$t_{\text{stress}} = t_{\text{initiation}} + \Delta t = \begin{cases} 11.25 + 0.48 = 11.73 \quad \text{(years)} \quad \text{(Constant model)} \\ 11.25 + 0.37 = 11.62 \quad \text{(years)} \quad \text{(Dynamic model)} \end{cases} \tag{25}$$

After the porous zone around the steel bar is completely filled with rust at t_{stress}, further corrosion progress will cause expansive stress and crack propagation in the surrounding concrete as illustrated in Figs. 2c and d.

Both the representative part of concrete slab in Fig. 7 and the finite element model in Fig. 8 are reserved to simulate the subsequent reinforcement rust expansion and concrete cracking. The corresponding displacement boundary conditions are illustrated in Fig. 11, where only vertical displacement is allowed on the left, right, front and rear surfaces of the slab, while all displacement constraints on the top and bottom surfaces are set free. The proposed corrosion-induced reinforcement rust expansion model is implemented by applying the transient radial displacement

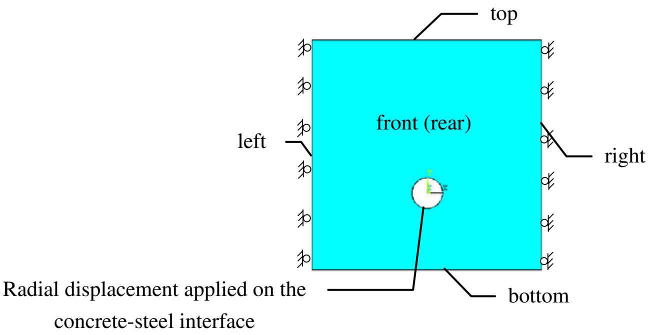

Fig. 11. Displacement boundary conditions.

on nodes along the concrete–steel interface. In addition, the two corrosion rate models – the constant model and the dynamic model – are introduced to model the reinforcement rust expansion and concrete cracking due to the chloride-induced corrosion.

The material properties of concrete used in this study are summarized in Table 2.

The total chloride content C_t, the temperature T and the ohmic resistance R_c at the depth of reinforcement after t_{stress} can still be excerpted from the previous simulation results in Figs. 9 and 10. Based on the dynamic corrosion rate model in Eq. (22), i_{corr} can be determined using C_t, T and R_c as shown in Fig. 12. It is observed that the fluctuation of i_{corr} is caused by the seasonal variation of temperature. Temperature has a significant effect on the corrosion rate, as with other chemical and electrochemical reactions. In addition, the mean value of the dynamic corrosion rate (0.012 A/m^2) is slightly higher than the constant corrosion rate (0.010 A/m^2), which implies that the assumed surface chloride boundary condition corresponds to the moderate corrosion risk and the dynamic corrosion rate model applies.

The two corrosion rate models produce two sets of simulation results. The diameter of the corroded steel bar D_{rb} and that of the rust expansion front D_{eb} are shown in Fig. 13. It can be observed that D_{rb} decreases monotonically with time, while D_{eb} increases monotonically with time. Meanwhile, D_{rb} and D_{eb} for the dynamic corrosion rate model are always less and greater than those for the constant corrosion rate model, since the mean value of the dynamic corrosion rate is higher than the constant corrosion rate.

The time-dependent radial displacement u_r is shown in Fig. 14, where the radial displacement increases monotonically with time, and the dynamic corrosion rate model predicts larger radial displacement than the constant corrosion rate model.

Since cracking is very sensitive to the transient stress state, the time step must be kept small enough to obtain a stable solution in simulating the crack propagation. In this simulation the time step is set as 0.02 year, while the entire time length after t_{stress} is chosen to be 1.0 year, only for the sake of illustration. To reflect the general varying trend of the number of cracked concrete elements, the fraction of cracked elements with the crack propagation process is demonstrated in Fig. 15. It can be observed that the two sets of crack propagation results are quite similar. Although the fraction of cracked elements increases monotonically with

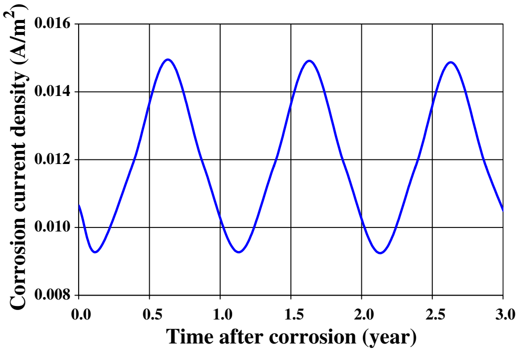

Fig. 12. Dynamic corrosion rate i_{corr}.

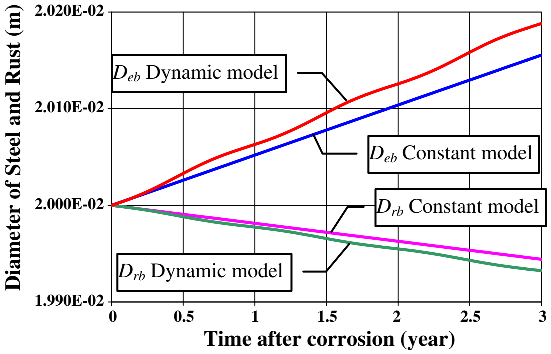

Fig. 13. D_{rb} and D_{eb}.

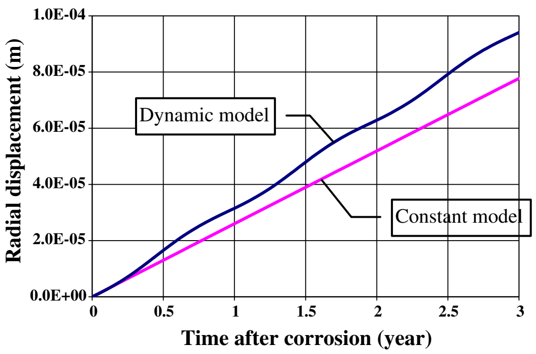

Fig. 14. Radial displacement boundary condition.

Table 2
Material properties of concrete

Compressive strength	$f'_c = 30$ MPa	Tensile strength	$f_t = 3$ MPa
Strain at peak stress	$\varepsilon_0 = 0.002$	Ultimate strain	$\varepsilon_{cu} = 0.003$
Elastic modulus	$E_c = 30$ GPa	Poisson's ratio	$\nu = 0.2$
Density	$\rho = 2400$ kg/m^3		

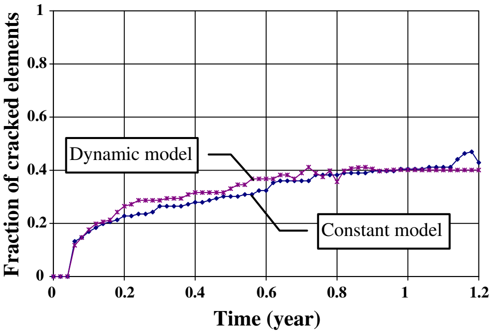

Fig. 15. Fraction of cracked concrete elements.

time, the distribution of cracks in the entire concrete slab is not uniform, and most cracks are localized closely around the steel bar. In addition, the fraction of cracked concrete elements gradually approaches a constant value, which helps to characterize some critical modes of structural failure, such as delamination or spalling of the concrete cover. Thus, the time to spalling t_{spalling} can be determined.

The crack propagation patterns caused by the reinforcement rust expansion can be observed in Fig. 16. For both corrosion rate models, cracks appear first at the same time $t = 0.06$ year after t_{stress} and the crack patterns looks similar to each other. Meanwhile, it is observed that the crack patterns agree well with the expectation in Fig. 2d, which verifies the feasibility of the proposed simulation methodology.

7. Discussion of simulation results

Several obvious crack paths can be found in Fig. 16, which indicates some possible crack propagation paths for the reinforced concrete slab under chloride-induced reinforcement corrosion. In addition, crushing due to compression is observed in those concrete elements closely around the steel bar, which is consistent with field observations.

One interesting phenomenon noticed is that two crack propagation paths along the horizontal direction proceed rapidly, while other crack paths progress relatively slowly. This observation confirms the experiment result by Dagher and Kulendran [46] that, for a concrete slab with closely spaced bars and thick concrete cover, cracks may grow and connect between the steel bars and form a delamination plane inside a slab. Once such a delamination plane forms, the entire concrete slab becomes an unstable structure. On the one hand, expansive stresses accumulated in concrete around the steel bar will be released rapidly. On the other hand, geometric deformation and displacement will increase rapidly. For a quasi-brittle material like concrete, it is difficult, if not impossible, to ensure the accuracy of the simulation results beyond this stage. As a result, few numerical models proposed so far are able to simulate accurately the crack propagation till the occurrence of delamination or spalling. The substantial contributions made earlier were predicting the time to crack initiation [5,8–10], which is much earlier than the occurrence of delamination and spalling. The proposed simulation methodology provides valuable information to

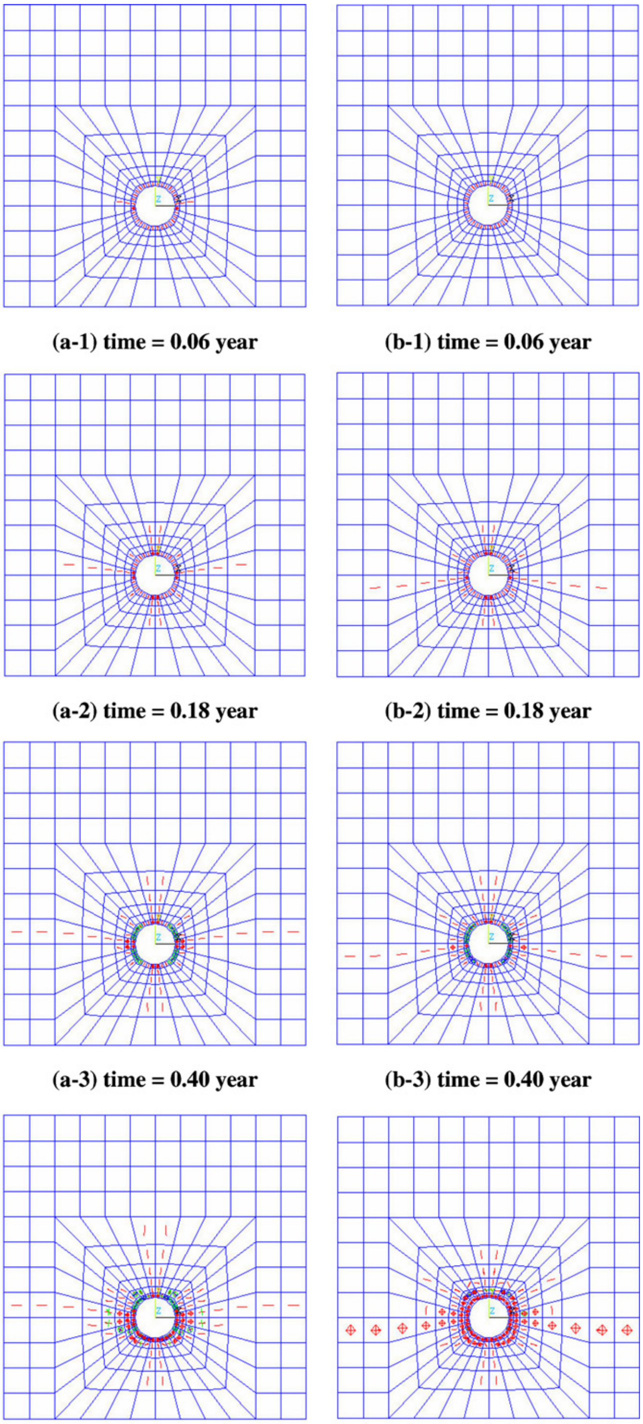
(a-1) time = 0.06 year
(b-1) time = 0.06 year
(a-2) time = 0.18 year
(b-2) time = 0.18 year
(a-3) time = 0.40 year
(b-3) time = 0.40 year
(a-4) time = 1.00 year
(b-4) time = 1.00 year

Fig. 16. Crack propagation patterns. (*Note:* 1. Series-a on left column for constant corrosion rate model, Series-b on right column for dynamic corrosion rate model; 2. The symbols | and ○ indicate different orientations of the cracks, and symbol ⊕ indicates multiple cracks distinguished with different colors.)

estimate the damage pattern and extent in concrete structures till the occurrence of delamination or spalling. Of course, the load carrying capacity of concrete structure at the time of delamination or spalling has been reduced so much that makes it hard to meet the design requirements.

The corrosion can be either pitting corrosion, where a very small anode is surrounded by a large area of cathode, or uniform corrosion with a homogeneous distribution of micro anodes and cathodes. Uniform corrosion may cause more overall loss in iron, but pitting corrosion causes more loss in cross-sectional area and hence is more dangerous. The proposed corrosion-induced reinforcement rust expansion model implies an assumption of uniform corrosion, without considering the pitting effect (i.e., localized corrosion). Uniform corrosion is usually encountered under carbonation or high chloride contamination, thus the applicability of the proposed model needs more verification. To overcome the difficulty of the pitting effect, it is possible to apply a user-defined uneven radial displacement around the steel-concrete interface as suggested by Dagher and Kulendran [46] and Stewart and Rosowsky [26]. However, the improvement is rather limited, and the whole simulation process is quite time consuming. More efforts are needed to consider the pitting effect, balancing computational effort and accuracy.

8. Conclusion

A finite element-based methodology is developed in this paper to simulate the entire degradation process from chloride penetration to reinforcement rust expansion to concrete cracking. The reinforcement corrosion model is based on Faraday's law, and the rust expansion is represented in the finite element analysis by an equivalent time-varying radial displacement boundary condition. Two established corrosion rate models – the constant model and the dynamic model – are combined with the proposed method. The cracking simulation uses a smeared cracking approach. The simulation results and the predicted crack patterns for a reinforced concrete slab exposed to a constant chloride environment agree well with the expectation in Fig. 2. Although some limitations exist in the proposed simulation methodology, the simplified approach can be used to a large extent to model the chloride-induced deterioration process of reinforced concrete structures.

Further work is needed to include to consider the influence of pitting corrosion in the proposed computational methodology. Many of the variables describing the structure, materials, environment, and the degradation process are random in nature. These uncertainties need to be properly accounted for in service life estimation, through systematic time-dependent probabilistic analysis. Sensitivity analysis to identify the dominant variables and to quantify their influence is valuable, both to reduce the computational effort, and to guide design decisions.

Acknowledgements

This study was supported by the US Department of Energy through the Consortium for Risk Evaluation with Stakeholder Participation (CRESP II). The support is gratefully acknowledged.

References

[1] Page CL, Treadaway KWJ. Aspects of electrochemistry of steel in concrete. Nature 1982;297:109–15.

[2] Townsend HE, Cleary HJ, Allegra L. Breakdown of oxide films in steel exposure to chloride solutions. NACE Corros 1981;37:384–91.

[3] Verbeck GJ. Mechanism of corrosion in concrete. In: Corrosion of metals in concrete. ACI SP-49; 1975.

[4] Mehta PK. Concrete structure properties and materials. Prentice-Hall, Inc.; 1993.

[5] Liu Y, Weyers RE. Modeling the time-to-corrosion cracking in chloride contaminated reinforced concrete structures. ACI Mater J 1998;95(6):675–81.

[6] Tuutti K. Corrosion of steel in concrete. Stochkolm, Sweden: Swedish Cement and Concrete Research Institute; 1982.

[7] Cady PD, Weyers RE. Chloride penetration and the deterioration of concrete bridge decks. Cement Concr Aggr 1983;5(2):81–7.

[8] Bazant ZP. Physical model for steel corrosion in sea structures – theory. J Struct Div 1979(June):1137–53.

[9] Bazant ZP. Physical model for steel corrosion in sea structures – applications. J Struct Div 1979(June):1153–66.

[10] Morinaga S. Prediction of service lives of reinforced concrete buildings based on rate of corrosion of reinforcing steel. In: Proceedings of building materials and components, Brighton, UK; 1990. p. 5–16.

[11] Xi Y, Bazant ZP. Modeling chloride penetration in saturated concrete. J Mater Civil Eng 1999;11(1):58–65.

[12] Martin-Perez B, Zibara H, Hooton RD, Thomas MDA. A study of the effect of chloride binding on service life prediction. Cement Concr Res 2000;30(8):1215–23.

[13] Nilsson LO, Massat M, Tang L. Chloride binding capacity and binding isotherms of OPC pastes and mortars. Cement Concr Res 1993;23(2):247–53.

[14] Onyejekwe OO, Reddy N. A numerical approach to the study of chloride ion penetration into concrete. Mag Concr Res 2000;52(4):243–50.

[15] Snyder KA. Validation and modification of the 4SIGHT Computer Program. NISTIR 6747; 2001.

[16] Martin-Perez B, Pantazopoulou SJ, Thomas MDA. Numerical solution of mass transport equations in concrete structures. Comput Struct 2001;79(13):1251–64.

[17] Kong JS, Ababneh AN, Frangopol DM, Xi Y. Reliability analysis of chloride penetration in saturated concrete. Probabilist Eng Mech 2002;17(3):305–15.

[18] Schiessl P. Corrosion of steel in concrete. RILEM Technical Committee 60-CSC. New York: Chapman and Hall; 1988.

[19] Elsener B. Corrosion of steel in concrete. In: Schutze M, editor. Corrosion and environmental degradation, vol. II. Wiley-VCH Weinheim; 2000. p. 389–436.

[20] Pantazopoulou SJ, Papoulia KD. Modeling cover-cracking due to reinforcement corrosion in RC structures. J Eng Mech 2001;127(4):342–51.

[21] Thoft-Christensen P. Stochastic modeling of the crack initiation time for reinforced concrete structures. In: Proceedings of 2000 ASCE structures congress, Philadelphia, USA; 2000.

[22] Jung WY, Yoon YS, Sohn YM. Predicting the remaining service life of land concrete by steel corrosion. Cement Concr Res 2003;33(5):663–77.

[23] Andrade C, Alonso C, Molina FJ. Covering cracking as a function of rebar corrosion: Part I – experimental test. Mater Struct 1993;26: 453–64.

[24] Hansen EJ, Saouma VE. Numerical simulation of reinforced concrete deterioration: Part II – steel corrosion and concrete cracking. ACI Mater J, Title no. 96-M41, 1999;331–7.

[25] Hong HP. Assessment of reliability of aging reinforced concrete structures. ASCE J Struct Eng 2000;126(12):1458–65.

[26] Stewart MG, Rosowsky DV. Time-dependent reliability of deteriorating reinforced concrete bridge decks. Struct Safety 1998;20(1): 91–109.

[27] Liu Y, Weyers RE. Modeling the dynamic corrosion process in chloride contaminated concrete structures. Cement Concr Res 1998;28(3):365–79.

[28] Liu Y. Modeling the time-to-corrosion cracking of the cover concrete in chloride contaminated reinforced concrete structures. Ph.D. dissertation, Virginia Polytechnic Institute; 1996.

[29] Thoft-Christensen P. Estimation of the service life time of concrete bridges. In: Proceedings of ASCE structures congress XV, Portland OR, USA; 1997.

[30] Thoft-Christensen P. Corrosion crack based assessment of the life-cycle reliability of concrete structures. In: Proceedings of ICOSSAR'01, Newport Beach, CA, USA; 2001.

[31] Thoft-Christensen P. What happens with reinforced concrete structures when the reinforcement corrodes? In: Proceedings of the 2nd international workshop on "Life-cycle cost analysis and design of civil infrastructure systems", Ube, Yamaguchi, Japan; 2001. p. 35–46.

[32] Shah SP, Swartz SE, Ouyang C. Fracture mechanics of concrete. New York: Wiley; 1995.

[33] Bazant ZP, Planas J. Fracture and size-effect in concrete and quasi-brittle materials. Boca Raton and London: CRC Press; 1998.

[34] Darwin D. Reinforced concrete. In: Finite element analysis of reinforced-concrete. Structures vol. II: Proceedings of the international workshop. New York: ASCE; 1993. p. 203–32.

[35] Mandke JS, Smalley AJ. Parameter studies for enhanced integrity of reciprocating compressor foundation blocks. Mechanical and fluids engineering division, Southwest Research Institute. Technical Report No. TA 94-1; 1994.

[36] Kachlakev D, Miller T, Yim S. Finite element modeling of reinforced concrete structures strengthened with FRP laminates. Final Report SPR 316 for Oregon Department of Transportation and Federal Highway Administration; 2001.

[37] Saouma VE, Chang S-Y. Numerical simulation of reinforced concrete deterioration due to steel corrosion, freezing–thawing and mechanical load effects. In: Frangopol DM, Bruhwiler E, Faber MH, Adey B, editors. Life-cycle performance of deteriorating structures: assessment, design and management. ASCE; 2003.

[38] ANSYS. ANSYS 7.0 Help, ANSYS Inc., Canonsburg, PA; 2002.

[39] Desayi P, Krishnan S. Equation for stress strain curve of concrete. J Am Concr Instit 1964;61:345–50.

[40] Hognestad EA. A study of combined bending and axial load in reinforced concrete members. Bulletin No. 399, Engineering Experiment Station, University of Illinois, Urbana, IL, vol. 49 (22); 1951.

[41] Willam KJ, Warnke EP. Constitutive model for the triaxial behavior of concrete. Proceedings international association for bridge and structural engineering, vol. 19. Bergamo Italy: ISMES; 1975. p. 174.

[42] Schiessl P, Raupach M. Influence of concrete composition and microclimate on the critical chloride content in concrete. In: Page CL, Threadaway KWJ, Bamforth PB, editors. Corrosion of Reinforcement in Concrete. London: Society of Chemical Industry, Elsevier Applied Science; 1990. p. 49–58.

[43] Hansson CM, Sorensen B. Threshold concentration of chloride in concrete for the initiation of reinforcement corrosion. In: Berke NS, Chaker V, Whiting D, editors. Corrosion rates of steel in concrete. ASTM STP 1065. Philadelphia, PA: American Society for Testing and Materials; 1990. p. 3–16.

[44] Berman HA. Sodium chloride corrosion of reinforcing steel and the pH of calcium hydroxides solution. ACI J 1975:587–98.

[45] Clear KC. Chloride at the threshold. Report of Kenneth C. Clear Inc.; 1983. p. 1011.

[46] Dagher HJ, Kulendran S. Finite element modeling of corrosion damage in concrete structures. ACI Struct J, Title no. 89-S67, 1992;699–708.